J|A|C|S ARTICLES

Published on Web 12/15/2009

In Situ XAS and XRPD Parametric Rietveld Refinement To Understand Dealumination of Y Zeolite Catalyst

Giovanni Agostini,[†] Carlo Lamberti,*[,†] Luca Palin,[‡] Marco Milanesio,[‡] Nadiya Danilina,[||] Bin Xu,[||] Markus Janousch,[§] and Jeroen A. van Bokhoven*[,||]

Department of Inorganic, Materials and Physical Chemistry, Torino University, Via P. Giuria 7, 10125 Turin, Italy, INSTM Unità di Torino Università, Turin, Italy, NIS Centre of Excellence, Università di Torino, Italy, Dipartimento di Scienze e Tecnologie Avanzate and Nano-SiSTeMI Interdisciplinary Centre, Università del Piemonte Orientale "A. Avogadro", Via T. Michel 11, 15121 Alessandria, Italy, Swiss Light Source, Paul Scherrer Institut, 5232 Villigen PSI, Switzerland, and ETH Zurich, Institute for Chemical and Bioengineering, HCI E127 8093 Zurich, Switzerland

Received September 10, 2009; E-mail: carlo.lamberti@unito.it; j.a.vanbokhoven@chem.ethz.ch

Abstract: Dealumination of NH_4−Y zeolite during steaming to 873 K was investigated with in situ, time-dependent, synchrotron radiation XRPD and in situ Al K-edge XAS. Water desorption is complete at 450 K, and ammonium decomposition occurs between 500 and 550 K. Only a small fraction of Al^{3+} species (5%) leaves the framework during heating from 710 to 873 K; these species occupy site **I′** inside the sodalite cage. This fraction increases up to 8% in the first 50 min at 873 K and remains constant for the following 70 min isotherm and during the high-temperature part of the cooling experiment. During cooling from 500 to 450 K, the electron density at site **I′** increases suddenly, corresponding to a fraction of 30−35% of the total Al, confirmed by ex situ ^{27}Al MAS solid-state NMR. At that temperature, in situ Al K-edge XAS indicates a change in Al coordination of a large fraction of Al, and thermogravimetric (TG) data show the first water molecules start to repopulate the pores. Such molecules drive the dislodgment of most of the Al from the zeolitic framework. Our data indicate that considerable structural collapse caused by steaming does not occur at the highest temperature; however, defects form, which lead to significant migration of framework Al^{3+} to extraframework positions, which occurs only as water is able to enter the pores again, that is, at much lower temperature. Contrary to general opinion, these results demonstrate that zeolite dealumination is not primarily a high-temperature process. The standard Rietveld refinement approach failed to identify extraframework Al species. These new results were obtained by adopting the innovative parametric refinement [*J. Appl. Crystallogr.* **2007**, *40*, 87]. Treating all of the XRPD patterns collected during the evolution of temperature as one unique data set significantly reduces the overall number of optimized variables and, thus, their relative correlation, and finally results in a more reliable estimate of the optimized parameters. Our results contribute to a better understanding of the phenomena involved on the atomic scale in the preparation of ultrastable Y zeolites (USY). USY are employed in fluid catalytic cracking (FCC), which is the most important conversion process in petroleum refineries to convert the high-boiling hydrocarbon fractions of petroleum crude oils to more valuable products like gasoline and olefinic gases.

1. Introduction

Zeolites find wide application in the chemical industry. They are microporous crystalline silica−alumina frameworks and have very large surface areas. Catalytically active sites in zeolites are often Brønsted acid sites, which are formed by a hydroxyl group that bridges framework Al and Si atoms. Both of these atoms are tetrahedrally coordinated. Because of their unique properties, such as form selectivity, high porosity, and thermal stability,[1−4] zeolites are active catalysts in many industrial acid-catalyzed reactions. Their activity and stability can be enhanced by different treatments, such as steaming, ion-exchange, and treatment with gaseous ammonia. During these treatments, the zeolite undergoes structural modification, such as Al migration into extraframework position and formation of mesopores. This benefits catalytic application of the material in industrial plants. To a certain extent, in all zeolitic frameworks a fraction of Al^{3+} species shows particularly low stability, which leads to a tendency for them to migrate into an extraframework position during the catalyst lifetime. As this process causes the loss of the corresponding Brønsted sites, the activity of the catalyst changes considerably with time. To overcome this, ultra stable zeolites were developed by subjecting the material to prolonged steaming to remove the more unstable Al^{3+} species. This leads to a catalyst with a high activity, which is stable in high-temperature reactions.[2,5−10] Of all of the catalytic applications of ultra stable zeolite Y, the most important is fluid catalytic

[†] University of Turin and NIS.
[‡] Università del Piemonte Orientale "A. Avogadro".
[§] Paul Scherrer Institut.
[||] ETH Zurich.

(1) Davis, M. E. *Acc. Chem. Res.* **1993**, *26*, 111–115.
(2) Corma, A.; Martinez, A. *Catal. Rev.—Sci. Eng.* **1993**, *35*, 483–570.

cracking (FCC) of the high-boiling hydrocarbon fraction of petroleum crude oil, which is converted to more valuable gasoline, olefinic gases, and other products.[11−21] Furthermore, the mesopore network, formed during steaming, improves the transport properties of the catalyst and, thus, its overall efficiency.[22] Despite the tremendous impact of the steam activation of zeolites, the dealumination process is still not clearly understood, probably because of its complexity and because we are dealing with an ordered/disordered transition, which is intrinsically difficult to monitor by means of crystallography.

X-ray powder diffraction (XRPD) is generally used to determine the crystal structure and the zeolite structure type.[23,24] The framework Al in crystalline zeolites has a symmetric tetrahedral coordination when moisture is present in the pores. Steamed zeolites have a large fraction of octahedral, distorted tetrahedral, and five-coordinated Al and have a lower crystallinity than unsteamed zeolites. ^{27}Al MAS solid-state NMR is generally used to determine the Al coordination, which can be done with high resolution and quantitatively. However, to enhance the resolution, samples are stored in a wet environment before measurement; measuring under dry conditions significantly broadens the spectra because of quadrupolar broadening. Acid zeolites are unstable in a moist atmosphere, and, during such simple treatment, structural changes occur and octahedrally coordinated Al forms.[25−27] The Al coordination is further affected by temperature; with increasing temperature, octahedrally coordinated Al becomes tetrahedrally coordinated, and, at high-temperature, 3-fold coordinated Al forms.[25] Steaming zeolite Y and measuring in a dry environment revealed tetrahedrally coordinated Al, indicating that moisture and temperature strongly affect the Al coordination.[26]

To understand the processes that take place during steam activation of a zeolite, in situ structural analysis is required. Here, we present the results of in situ time-resolved XRPD and in situ Al K-edge X-ray absorption spectroscopy (XAS). XRPD gives the long-range structure and XAS the local Al coordination.[28] Because both methods can be performed in situ, a complete picture of the evolution of the Al species as well as of their framework and extraframework characteristics can be determined. The value of combining diffraction and complementary in situ techniques has been widely demonstrated.[29−48]

The time-resolved synchrotron XRPD yields many consecutive patterns, which we analyzed simultaneously by means of

(3) De Vos, D. E.; Dams, M.; Sels, B. F.; Jacobs, P. A. *Chem. Rev.* **2002**, *102*, 3615–3640.
(4) Sartori, G.; Maggi, R. *Chem. Rev.* **2006**, *106*, 1077–1104.
(5) Martens, J. A.; Parton, R.; Uytterhoeven, L.; Jacobs, P. A.; Froment, G. F. *Appl. Catal.* **1991**, *76*, 95–116.
(6) Wang, J.; Park, J. N.; Park, Y. K.; Lee, C. W. *J. Catal.* **2003**, *220*, 265–272.
(7) Corma, A.; Fornes, V.; Navarro, M. T.; Perezpariente, J. *J. Catal.* **1994**, *148*, 569–574.
(8) Corma, A.; Grande, M. S.; GonzalezAlfaro, V.; Orchilles, A. V. *J. Catal.* **1996**, *159*, 375–382.
(9) Xu, B.; Bordiga, S.; Prins, R.; van Bokhoven, J. A. *Appl. Catal., A* **2007**, *333*, 245–253.
(10) Williams, M. F.; Fonfe, B.; Sievers, C.; Abraham, A.; van Bokhoven, J. A.; Jentys, A.; van Veen, J. A. R.; Lercher, J. A. *J. Catal.* **2007**, *251*, 485–496.
(11) Beyerlein, R. A.; ChoiFeng, C.; Hall, J. B.; Huggins, B. J.; Ray, G. J. *Top. Catal.* **1997**, *4*, 27–42.
(12) Kuehne, M. A.; Kung, H. H.; Miller, J. T. *J. Catal.* **1997**, *171*, 293–304.
(13) Kuehne, M. A.; Babitz, S. M.; Kung, H. H.; Miller, J. T. *Appl. Catal., A* **1998**, *166*, 293–299.
(14) Williams, B. A.; Babitz, S. M.; Miller, J. T.; Snurr, R. Q.; Kung, H. H. *Appl. Catal., A* **1999**, *177*, 161–175.
(15) Babitz, S. M.; Williams, B. A.; Miller, J. T.; Snurr, R. Q.; Haag, W. O.; Kung, H. H. *Appl. Catal., A* **1999**, *179*, 71–86.
(16) Sanchez-Castillo, M. A.; Agarwal, N.; Miller, C.; Cortright, R. D.; Madon, R. J.; Dumesic, J. A. *J. Catal.* **2002**, *205*, 67–85.
(17) Yan, Z. M.; Ding, M. A.; Zhuang, J. Q.; Liu, X. C.; Liu, X. M.; Han, X. W.; Bao, X. H.; Chang, F. X.; Xu, L.; Liu, Z. M. *J. Mol. Catal. A* **2003**, *194*, 153–167.
(18) Katada, N.; Nakata, S.; Kato, S.; Kanehashi, K.; Saito, K.; Niwa, M. *J. Mol. Catal. A* **2005**, *236*, 239–245.
(19) Niwa, M.; Suzuki, K.; Isamoto, K.; Katada, N. *J. Phys. Chem. B* **2006**, *110*, 264–269.
(20) Corma, A.; Huber, G. W.; Sauvanaud, L.; O'Connor, P. *J. Catal.* **2007**, *247*, 307–327.
(21) Cerqueira, H. S.; Caeiro, G.; Costa, L.; Ribeiro, F. R. *J. Mol. Catal. A* **2008**, *292*, 1–13.
(22) Kortunov, P.; Vasenkov, S.; Karger, J.; Valiullin, R.; Gottschalk, P.; Elia, M. F.; Perez, M.; Stocker, M.; Drescher, B.; McElhiney, G.; Berger, C.; Glaser, R.; Weitkamp, J. *J. Am. Chem. Soc.* **2005**, *127*, 13055–13059.
(23) Baerlocher, C.; McCuster, L. B.; Olson, D. H. *Atlas of Zeolite Framework Types*, 6th revised ed.; Elsevier: Amsterdam, 2007.
(24) Treacy, M. M. J.; Higgins, J. B. *Collection of Simulated XRD Powder Patterns for Zeolites*, 5th revised ed.; Elsevier: Amsterdam, 2007.
(25) van Bokhoven, J. A.; van der Eerden, A. M. J.; Koningsberger, D. C. *J. Am. Chem. Soc.* **2003**, *125*, 7435–7442.
(26) Altwasser, S.; Jiao, J.; Steuernagel, S.; Weitkamp, J.; Hunger, M. *Stud. Surf. Sci. Catal.* **2004**, *154*, 3098–3105.
(27) van Bokhoven, J. A. *Phys. Scr.* **2005**, *T115*, 76–79.
(28) van Bokhoven, J. A.; Sambe, H.; Ramaker, D. E.; Koningsberger, D. C. *J. Phys. Chem. B* **1999**, *103*, 7557–7564.
(29) Couves, J. W.; Thomas, J. M.; Waller, D.; Jones, R. H.; Dent, A. J.; Derbyshire, G. E.; Greaves, G. N. *Nature* **1991**, *354*, 465–468.
(30) Sankar, G.; Wright, P. A.; Natarajan, S.; Thomas, J. M.; Greaves, G. N.; Dent, A. J.; Dobson, B. R.; Ramsdale, C. A.; Jones, R. H. *J. Phys. Chem.* **1993**, *97*, 9550–9554.
(31) Clausen, B. S.; Grabaek, L.; Steffensen, G.; Hansen, P. L.; Topsoe, H. *Catal. Lett.* **1993**, *20*, 23–36.
(32) Marra, G. L.; Fitch, A. N.; Zecchina, A.; Ricchiardi, G.; Salvalaggio, M.; Bordiga, S.; Lamberti, C. *J. Phys. Chem. B* **1997**, *101*, 10653–10660.
(33) Grey, C. P.; Poshni, F. I.; Gualtieri, A. F.; Norby, P.; Hanson, J. C.; Corbin, D. R. *J. Am. Chem. Soc.* **1997**, *119*, 1981–1989.
(34) Norby, P.; Poshni, F. I.; Gualtieri, A. F.; Hanson, J. C.; Grey, C. P. *J. Phys. Chem. B* **1998**, *102*, 839–856.
(35) Palomino, G. T.; Bordiga, S.; Zecchina, A.; Marra, G. L.; Lamberti, C. *J. Phys. Chem. B* **2000**, *104*, 8641–8651.
(36) Masciocchi, N.; Bruni, S.; Cariati, E.; Cariati, F.; Galli, S.; Sironi, A. *Inorg. Chem.* **2001**, *40*, 5897–5905.
(37) Milanesio, M.; Artioli, G.; Gualtieri, A. F.; Palin, L.; Lamberti, C. *J. Am. Chem. Soc.* **2003**, *125*, 14549–14558.
(38) Turco, M.; Bagnasco, G.; Costantino, U.; Marmottini, F.; Montanari, T.; Ramis, G.; Busca, G. *J. Catal.* **2004**, *228*, 43–55.
(39) Grandjean, D.; Beale, A. M.; Petukhov, A. V.; Weckhuysen, B. M. *J. Am. Chem. Soc.* **2005**, *127*, 14454–14465.
(40) Mesu, J. G.; van der Eerden, A. M. J.; de Groot, F. M. F.; Weckhuysen, B. M. *J. Phys. Chem. B* **2005**, *109*, 4042–4047.
(41) Martucci, A.; Alberti, A.; Cruciani, G.; Frache, A.; Marchese, L.; Pastore, H. O. *J. Phys. Chem. B* **2005**, *109*, 13483–13492.
(42) Beale, A. M.; van der Eerden, A. M. J.; Jacques, S. D. M.; Leynaud, O.; O'Brien, M. G.; Meneau, F.; Nikitenko, S.; Bras, W.; Weckhuysen, B. M. *J. Am. Chem. Soc.* **2006**, *128*, 12386–12387.
(43) (a) Boccaleri, E.; Carniato, F.; Croce, G.; Viterbo, D.; van Beek, W.; Emerich, H.; Milanesio, M. *J. Appl. Crystallogr.* **2007**, *40*, 684–693.
(44) Sankar, G.; Okubo, T.; Fan, W.; Meneau, F. *Faraday Discuss.* **2007**, *136*, 157–166.
(45) (a) Goto, Y.; Sato, H.; Shinkai, S.; Sada, K. *J. Am. Chem. Soc.* **2008**, *130*, 14354–14355. (b) Cavka, J. H.; Jakobsen, S.; Olsbye, U.; Guillou, N.; Lamberti, C.; Bordiga, S.; Lillerud, K. P. *J. Am. Chem. Soc.* **2008**, *130*, 13850–13851.
(46) O'Brien, M. G.; Beale, A. M.; Jacques, S. D. M.; Buslaps, T.; Honkimaki, V.; Weckhuysen, B. M. *J. Phys. Chem. C* **2009**, *113*, 4890–4897.
(47) de Smit, E.; Beale, A. M.; Nikitenko, S.; Weckhuysen, B. M. *J. Catal.* **2009**, *262*, 244–256.
(48) Kumar, S.; Carniato, F.; Arrais, A.; Croce, G.; Boccaleri, E.; Palin, L.; van Beek, W.; Milanesio, M. *Cryst. Growth Des.* **2009**, *9*, 3396–3404.

parametric analysis. This enhanced the reliability of the results.[49] Standard Rietveld refinement[50,51] of time-resolved XRPD patterns is performed by considering each individual pattern as an independent acquisition.[30,31,33,34,37,39−44,48,52−73] This means that all of the refined parameters, such as scale factor, background factors, and position and occupancy of the atom, in two subsequent patterns are refined independently. This approach is ideal when dealing with single crystal data, which have very high data/parameter ratio, but can be problematic when referring to time-resolved XRPD data, where the S/N quality of a pattern is significantly lower with respect to static acquisition. In a time-resolved study, the structure usually evolves gradually and undergoes small changes after two consecutive acquisitions. This can be exploited to limit the parameter space by applying restraints. For instance, parameters, which behave predictably, such as an exponential decay of the known lifetime of the scale factor due to the current decay of the synchrotron source and a linear evolution of the atomic position of framework atoms due to thermal expansion, can be parametrized by Rietveld refinement of the series according to some expected evolution. This will reduce the bias due to the low data/parameter ratio typical of in situ XRPD. In this way, the set of N diffraction patterns of the time-resolved series is treated as a unique and consistent set of data, allowing us to significantly increase the statistics, to reduce the overall number of optimized variables and, thus, their relative correlation, and finally to obtain a more reliable estimate of the optimized parameters.

A remarkable improvement based on the refinement strategy has been demonstrated: a greater precision in the determination of cell parameters during thermal treatments[49,74,75] and in the structure determination of L-serine polymorphs from high-pressure neutron powder diffraction (0−8 GPa).[76] To the best of our knowledge, this is the first time that this method has been applied to zeolites. Its application and correlation to in situ XAS as well as ex situ ^{27}Al MAS NMR data enabled us to determine the evolution of the structural changes that occur during steam treatment of zeolite Y over various periods of time.

2. Experimental Methods

2.1. Materials. NH_4Y was obtained by triple ion exchange of NaY (LZ-Y54, UOP, Molecular Sieve Division) at 353 K with 1 M NH_4NO_3. The residual Na content was determined by atomic absorption spectroscopy (AAS) and accounted for <0.05% of the Al content. The Si/Al ratio was 2.6. The structure and properties of the sample are described elsewhere.[77]

2.2. Synchrotron XRPD, NMR, and XAS Data Collection. All synchrotron XRPD data were collected using an image plate (IP) detector at the GILDA BM8 beamline of ESRF[78] (Figure S1 of the Supporting Information). The wavelength was 0.48973(7) Å, calibrated against the lattice parameters of the NIST LaB_6 standard (SRM 660b; nominal a = 4.156 95(6) Å at room temperature). This calibration was also used to determine the sample-to-IP distance as well as the optimization of the parameters as required for the tilt corrections. The images were collected on the IP and were retrieved with a Fuji BAS2500 scanner. Three patterns were acquired at constant temperature according to Scheme 1: at room temperature, at the start (S1), and at the end (S3) of the experiment, and at the highest temperature (S2). The images were integrated into the complete diffraction ring to obtain the best possible signal/noise ratio. The absence of preferred orientation and texture was confirmed by the 2D diffraction images. The static XRPD patterns contained data up to $\sin(\theta)/\lambda = 0.52$, which corresponds to a d spacing of 0.96 Å.

The time-resolved X-ray diffraction patterns were accumulated continuously by the IP detector up to $\sin(\theta)/\lambda = 0.37$, which corresponds to a d spacing of 1.36 Å, in a translating system[37,62] (Figure S1). The time resolution, Δt, was defined by the translation speed of the IP detector and the opening of the slits and was 3 mm. Conventional intensity versus 2θ files were obtained by pixel integration of the image using software, especially developed for this purpose by the staff of GILDA. Patterns were collected during the temperature treatment (Scheme 1) heating from 300 to 873 K with 2.0 K/min and cooling with 4.8 K/min, resulting in ΔT = 11.5 K/pattern and ΔT = 21.5 K/pattern, respectively. The cooling rate was constant until about 500 K, after which the rate and ΔT decreased.

The thermal treatments were carried out using a Cyberstar gas blower, equipped with a Eurotherm 902b temperature controller; the gas blower was placed near the central part of the capillary (Figure S1a). The temperature was monitored by a thermocouple, in the opening of the furnace. In a separate experiment, the real temperature of the capillary was calibrated by monitoring the

(49) Stinton, G. W.; Evans, J. S. O. *J. Appl. Crystallogr.* **2007**, *40*, 87–95.
(50) Rietveld, H. M. *Acta Crystallogr.* **1967**, *22*, 151–152.
(51) Rietveld, H. M. *J. Appl. Crystallogr.* **1969**, *2*, 65–71.
(52) Cheetham, A. K.; Wilkinson, A. P. *Angew. Chem., Int. Ed. Engl.* **1992**, *31*, 1557–1570.
(53) Steel, A. T.; Dooryhee, E. *Zeolites* **1993**, *13*, 336–340.
(54) Artioli, G. *Nucl. Instrum. Methods Phys. Res., Sect. B* **1997**, *133*, 45–49.
(55) Cruciani, G.; Artioli, G.; Gualtieri, A.; Stahl, K.; Hanson, J. C. *Am. Mineral.* **1997**, *82*, 729–739.
(56) Norby, P. *J. Am. Chem. Soc.* **1997**, *119*, 5215–5221.
(57) Cruciani, G.; Gualtieri, A. *Am. Mineral.* **1999**, *84*, 112–119.
(58) Norby, P.; Hanson, J. C.; Fitch, A. N.; Vaughan, G.; Flaks, L.; Gualtieri, A. *Chem. Mater.* **2000**, *12*, 1473–1479.
(59) Artioli, G.; Stahl, K.; Cruciani, G.; Gualtieri, A.; Hanson, J. C. *Am. Mineral.* **2001**, *86*, 185–192.
(60) Ciraolo, M. F.; Hanson, J. C.; Norby, P.; Grey, C. P. *J. Phys. Chem. B* **2001**, *105*, 2604–2611.
(61) Lee, Y.; Reisner, B. A.; Hanson, J. C.; Jones, G. A.; Parise, J. B.; Corbin, D. R.; Toby, B. H.; Freitag, A.; Larese, J. Z. *J. Phys. Chem. B* **2001**, *105*, 7188–7199.
(62) Meneghini, C.; Artioli, G.; Balerna, A.; Gualtieri, A. F.; Norby, P.; Mobilio, S. *J. Synchrotron Radiat.* **2001**, *8*, 1162–1166.
(63) Walton, R. I.; Millange, F.; O'Hare, D.; Davies, A. T.; Sankar, G.; Catlow, C. R. A. *J. Phys. Chem. B* **2001**, *105*, 83–90.
(64) Kappen, P.; Troger, L.; Materlik, G.; Reckleben, C.; Hansen, K.; Grunwaldt, J. D.; Clausen, B. S. *J. Synchrotron Radiat.* **2002**, *9*, 246–253.
(65) Cruciani, G.; Martucci, A.; Meneghini, C. *Eur. J. Mineral.* **2003**, *15*, 257–266.
(66) Dalconi, M. C.; Alberti, A.; Cruciani, G. *J. Phys. Chem. B* **2003**, *107*, 12973–12980.
(67) Martorana, A.; Deganello, G.; Longo, A.; Deganello, F.; Liotta, L.; Macaluso, A.; Pantaleo, G.; Balerna, A.; Meneghini, C.; Mobilio, S. *J. Synchrotron Radiat.* **2003**, *10*, 177–182.
(68) Celestian, A. J.; Parise, J. B.; Goodell, C.; Tripathi, A.; Hanson, J. *Chem. Mater.* **2004**, *16*, 2244–2254.
(69) Loiseau, T.; Beitone, L.; Millange, F.; Taulelle, F.; O'Hare, D.; Ferey, G. *J. Phys. Chem. B* **2004**, *108*, 20020–20029.
(70) Cruciani, G. *J. Phys. Chem. Solids* **2006**, *67*, 1973–1994.
(71) Dalconi, M. C.; Cruciani, G.; Alberti, A.; Ciambelli, P. *Microporous Mesoporous Mater.* **2006**, *94*, 139–147.
(72) Martucci, A.; Guzman-Castillo, M. D. L.; Di Renzo, F.; Fajula, F.; Alberti, A. *Microporous Mesoporous Mater.* **2007**, *104*, 257–268.
(73) Merlini, M.; Gemmi, M.; Cruciani, G.; Artioli, G. *Phys. Chem. Miner.* **2008**, *35*, 147–155.
(74) Masciocchi, N.; Pettinari, C.; Alberti, E.; Pettinari, R.; Di Nicola, C.; Albisetti, A. F.; Sironi, A. *Inorg. Chem.* **2007**, *46*, 10491–10500.
(75) Khatko, V.; Mozalev, A.; Gorokh, G.; Solovei, D.; Guirado, F.; Llobet, E.; Correig, X. *J. Electrochem. Soc.* **2008**, *155*, K116–K123.
(76) Wood, P. A.; Francis, D.; Marshall, W. G.; Moggach, S. A.; Parsons, S.; Pidcock, E.; Rohl, A. L. *CrystEngComm* **2008**, *10*, 1154–1166.
(77) Xu, B.; Rotunno, F.; Bordiga, S.; Prins, R.; van Bokhoven, J. A. *J. Catal.* **2006**, *241*, 66–73.
(78) Pascarelli, S.; Boscherini, F.; Dacaptito, F.; Hrdy, J.; Meneghini, C.; Mobilio, S. *J. Synchrotron Radiat.* **1996**, *3*, 147–155.

Scheme 1. Temperature Evolution during Collection of in Situ XRPD Data[a]

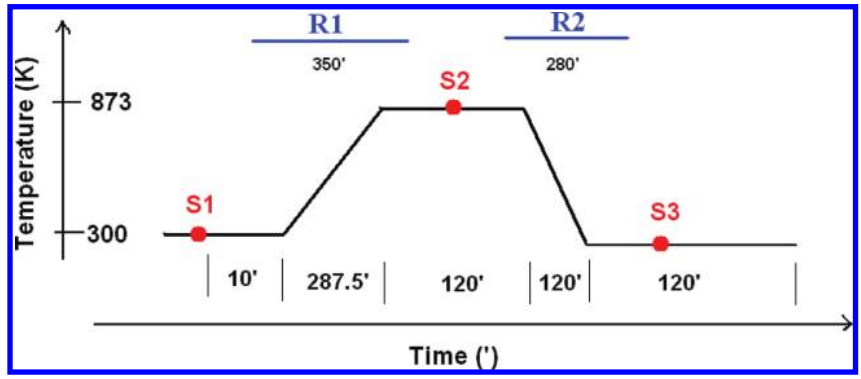

[a] Full image plate data (5′ of acquisition) were acquired at room temperature (S1) before starting the heating experiment (R1), in the middle of the isotherm at 873 K (S2), and at 300 K after cooling (S3). During the two time-/temperature-dependent ramps, R1 and R2, patterns were continuously collected.

expansion of the cell volume from 300 to 1000 K, revealed by Rietveld analysis of a silver wire. Of course, a small displacement in the position of the capillary or the blower might result in a systematic error in the estimated temperature of the zeolite powder. Such error is however considered a posteriori low according to the good agreement between XRPD and TGA data (vide infra Figure 7). Zeolite powder was ground and carefully packed in an open 1.0 mm quartz capillary between bundles of glass wool. The capillary was then mounted onto a T piece with a ferrule and placed on the goniometer head to allow simultaneous twisting of the sample to minimize the effect of preferential orientations and the flushing of gas through the capillary. After the capillary was bubbled through liquid water in a saturator, N_2 was flowed through the capillary. Any back-mixing of air that might occur to a small extent in the XRD capillary is not expected to significantly influence the amount of water that flows over the sample and will not affect the data.

Al K-edge XANES spectra were recorded at the Line for the Ultimate Characterizations by Imaging and Absorption (LUCIA)[79] at the Swiss Light Source (SLS) in Villigen, Switzerland, operating at 2.4 GeV with a ring current of 300 mA in top-up mode. A water-cooled double crystal KTP monochromator was used. Higher harmonics were reduced with a set of two flat and nickel-coated silicon mirrors at a variable incidence angle of 0.4−1.3°, which also reduced the heat on the monochromator crystals. Spectra were measured in transmission mode using a photodiode to detect the transmitted beam. The incident beam intensity was determined by measuring the total electron yield of a 200 nm thick nickel foil. The spectra were recorded in a specially designed in situ cell, through which gas flows through a pellet, a few micrometers thick, and which can be heated to 873 K. The in situ cell was placed inside a bag filled with helium, and Si_3N_4 windows, 50 nm thick, separated the contents in the cell from the helium in the bag. The vacuum of the beamline was protected by a Si_3N_4 window of 100 nm thickness attached to the end of the beamline. Data were analyzed according to standard procedures.

^{27}Al MAS NMR experiments were carried out with a Bruker Avance 700 NMR spectrometer using a 2.5 mm double-resonance probe-head. The resonance frequency for ^{27}Al was 182.4 MHz, and the pulse length was 6 μs. All of the spectra were obtained at a spinning speed of 15 kHz and had a recycle delay of 1 s. The ^{27}Al chemical shifts were referenced to the Al compound (NH_4)-$Al(SO_4)_2 \cdot 12H_2O$.

Samples of approximately 30 mg were treated in a Mettler Toledo TGA/SDTA851e instrument for thermogravimetric analysis (TGA). The sample was heated to 873 K with 2 K/min, kept at 873 K for 120 min, cooled to 298 K with −4.8 K/min, and kept at room temperature for 240 min. Helium, kept saturated by bubbling through water in a saturator, was passed over the sample at a flow of 50 mL/min throughout the measurement.

2.3. XRPD Refinement Strategy. Rietveld refinements[50,51] were performed using TOPAS-Academic V4.1 software.[80] At first, refinements were performed on the acquisitions that were taken at constant temperature (S1, S2, and S3, Scheme 1) because of their higher S/N ratio and larger 2θ range. S2 was analyzed first due to the negligible electron scattering density inside the cages, which enabled an accurate optimization of the atoms of the framework. The starting model was that of dehydrated H−Y, which was determined using neutron powder diffraction data.[81] The framework refinement was done by fixing the Si, Al, and O occupancy to 0.72, 0.28, and 1.0 according to the chemical analysis. The atom coordinates were varied. The isotropic temperature factors were expressed as B_{eq}, with the thermal correction to the structure factor being proportional to $\exp[B_{eq} \sin^2(\theta)/\lambda^2]$ ($1\ B_{eq} = 8\pi^2\ U_{iso}$). After some preliminary tests refining B_{eq}, the observed trend of B_{eq} versus temperature indicated that the thermal effects on B_{eq} that resulted were small, and therefore B_{eq}'s were kept fixed in the remaining refinements at $B_{eq}(Si) = B_{eq}(Al) = 1.5$ Å^2, $B_{eq}(O) = 3.0$ Å^2, and B_{eq}(extraframework atoms) = 5 Å^2, to avoid problems with correlation. These values agree well with those reported in the literature.[82] A modified Thompson−Cox−Hastings pseudo-Voigt profile function with a simple axial correction was used.[83] The background was fitted with an 18-parameter Chebychev polynomial function. The small extraframework electron scattering density following the thermal treatment (incompatible with the presence of H_2O or NH_4^+) was ascribed to Al atoms and localized by fixing the framework and applying the simulated annealing algorithm[84] implemented in TOPAS.[85,86] A final refinement was then performed

(79) Flank, A. M.; Cauchon, G.; Lagarde, P.; Bac, S.; Janousch, M.; Wetter, R.; Dubuisson, J. M.; Idir, M.; Langlois, F.; Moreno, T.; Vantelon, D. *Nucl. Instrum. Methods Phys. Res., Sect. B* **2006**, *246*, 269–274.

(80) Coelho, A. A. *J. Appl. Crystallogr.* **2005**, *38*, 455–461.

(81) Czjzek, M.; Jobic, H.; Fitch, A. N.; Vogt, T. *J. Phys. Chem.* **1992**, *96*, 1535–1540.

(82) Wozniak, A.; Marler, B.; Angermund, K.; Gies, H. *Chem. Mater.* **2008**, *20*, 5968–5976.

(83) Young, R. A. Introduction to the Rietveld Method. In *The Rietveld Method*; Young, R. A., Ed.; IUCr Book Series, Oxford University Press: Oxford, 1993; pp 1−39.

(84) In the simulated annealing algorithm implemented in TOPAS, the atom occupancies are refined and then atom positions are displaced by random amounts (scaled by a "temperature" factor; the higher is the virtual temperature, the higher are the random movements). This step is repeated up to convergence and finally the data refined again versus experimental data without any random movements, retaining the best *R*-factor solution sampled in the parameter space. Within TOPAS, the same approach may be applied to any refined parameter, if needed.

(85) Coelho, A. A. *J. Appl. Crystallogr.* **2000**, *33*, 899–908.

(86) Coelho, A. A. *Topas: Technical Reference*; http://members.optusnet.com.au/~alancoelho/, 2006.

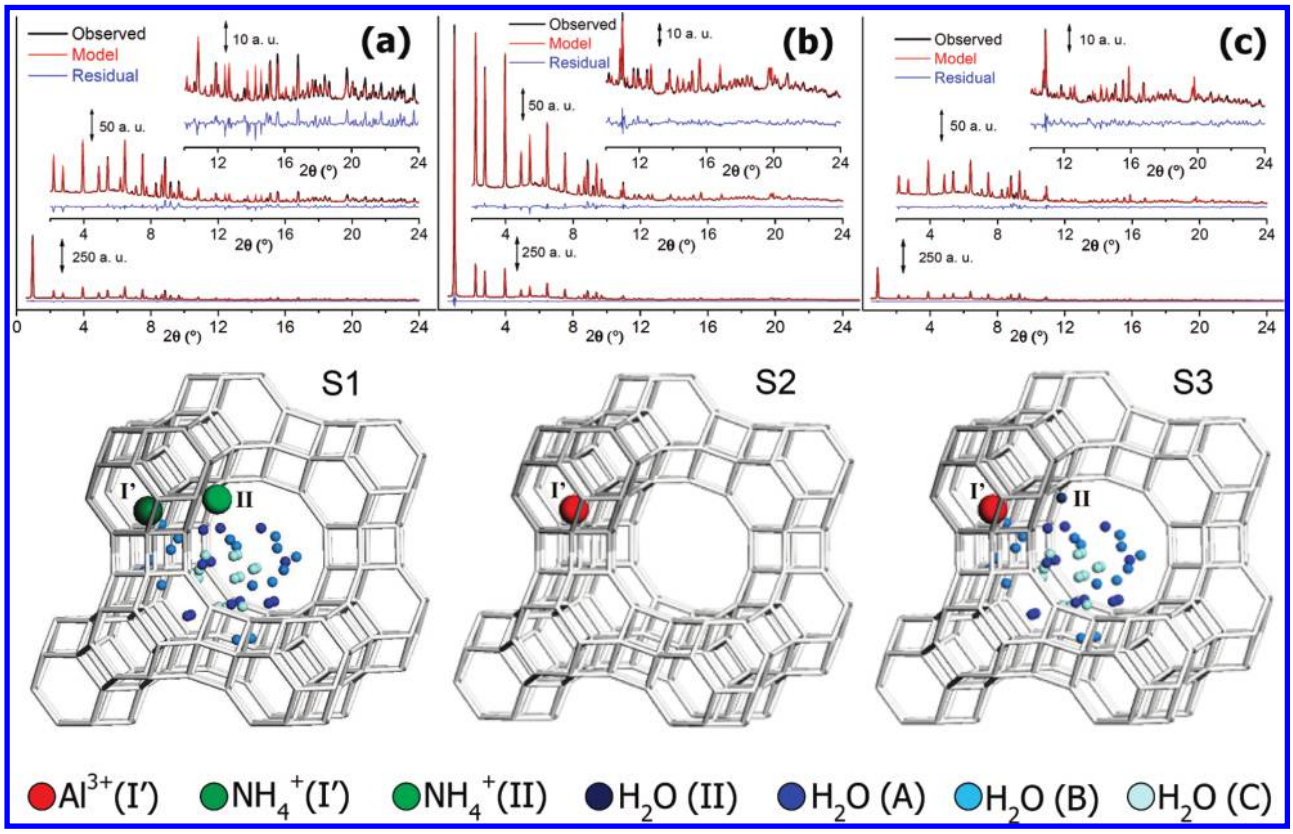

Figure 1. Refinements (top) and relative models (bottom) for the XRPD data, collected at various temperatures: 300 K, S1 (a); 873 K, S2 (b); 300 K, S3 (c). Top: Observed (black), calculated (red), and residual (blue) profiles. The zooms highlight the 2−24° and 10−24° 2θ regions to illustrate the quality of the data and the refinement. Bottom: Sticks representation of the Y zeolite framework showing one supercage and several sodalite cages together with the refined extraframework (I′, II) and water (A, B, and C) sites according to the models used in the refinement (Tables S1−S3 of the Supporting Information).

by allowing the depopulation of framework Al sites correlated to the appearance of the new extraframework phase (vide infra Figure 1b).

The same strategy was adopted to refine the S1 and S3 patterns (Scheme 1), in which water and ammonium are the unique (S1) or predominant (S3) species and explain the extraframework electron density. For this reason, the simulated annealing procedure was performed by optimizing five and four extraframework positions and relative occupancy for S1 and S3. All of the parameters defining the profile function, coordinates of the extraframework positions, and B_{eq} were first optimized in the static patterns and were then fixed in all refinements done on the patterns collected in the dynamic experiments. This strategy enabled the minimizing of the correlation coefficients of scale factor, occupancy factors, and thermal displacement parameters without adding bias.

The diffraction patterns collected during heating and cooling were first refined by considering each diffractogram as an independent data set. With this approach, we determined those parameters, which behaved in a physically predictable manner during the dynamic experiment. This was the case for the scale value and the coordinates of the framework atoms. The variation in such parameters (P) was then parametrized according to $P(i) = a*i + P_0$, where i represents the number of diffractograms (from 0 to 61), P_0 the starting value of the parameter, and a the slope that defines the variation in the series. With the standard approach, 62 independent $P(i)$ parameters could be optimized as compared to only two (a, P_0) with parametrization. Successively, a second refinement step was executed by adopting the parametrization for the scale factor and the framework atom coordinates.[49] This means that the remaining parameters (cell parameter, extraframework site occupancy, and background factors) were independent during the refinement. The evolution of the occupancy factors of the different extraframework sites as a function of temperature enabled the assignment of the atoms or molecules (H_2O, NH_4^+, or Al^{3+}) to the observed electron density. A final parametric refinement was performed by attributing the correct atom for each extraframework site to obtain the final occupancy factors as a function of temperature.

3. Results

3.1. Synchrotron XRPD Data Collection. Figure 1 illustrates the good quality of the data (black curves) and of the refinement (red curves) for the static patterns collected at points S1, S2, and S3 of Scheme 1. The unit cell parameters, quality factors, atomic positions, occupancy factors, B_{eq}, and atoms per unit cells obtained from each refinement are reported in Tables S1−S3 of the Supporting Information.

Figure 2a and b reports the evolution of the XRPD patterns collected during R1 and R2, respectively (Scheme 1). The large intensity increase in the low 2θ reflections, which was observed in the heating experiment at around 400 K, reflects an electron scattering density drop inside the channels, caused by water desorption. The reverse change in the intensity was more pronounced for R2, suggesting that water readsorption was not the only process involved as confirmed by the refinement of the extraframework electron density peaks (see Discussion).

Along both heating and cooling experiments, no significant increase of the fwhm of the peak profile was observed (0.6° for the low θ reflections). This means that the overall amorphization process is negligible, further confirming that keeping B_{eq} values fixed was a realistic approximation. This fact well

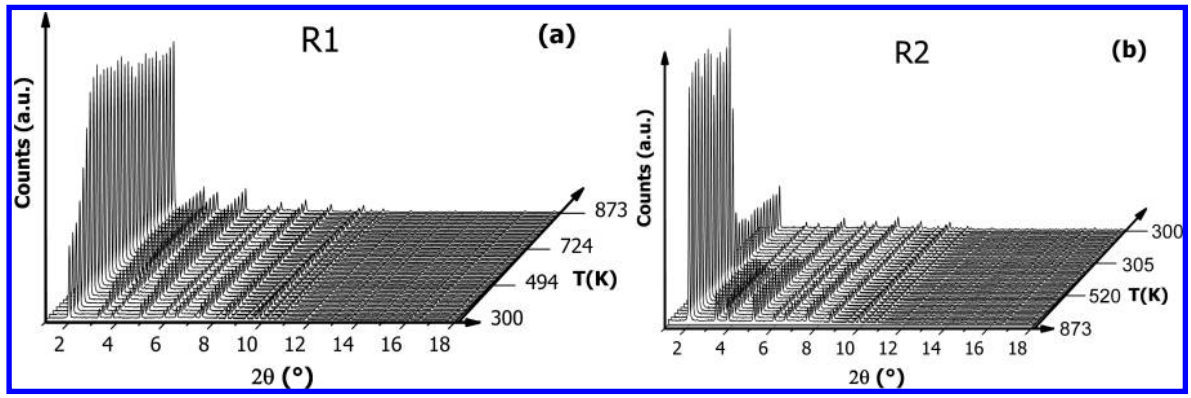

Figure 2. Three-dimensional representation of the XRPD patterns collected during the heating (R1, part a) and cooling (R2, part b) experiments. The decrease in the low θ reflection during R2 (zeolite rehydration) was much more abrupt than the more gradual increase during R1 (zeolite dehydration). R1 was performed with a gradient of $+2$ K/min^{-1}, while R2 was performed with a nominal gradient of -4.8 K/min^{-1}: This gradient holds in the high-temperature range only; the sample follows a much smoother, exponential-like temperature decay due to the huge thermal inertia of the gas blower (see text and Supporting Information for more details).

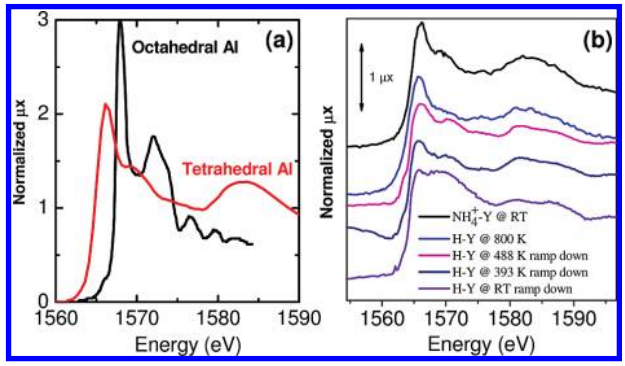

Figure 3. Al K-edge XANES spectra. (a) α-Al_2O_3 (black curve) and Na$-$Y (red curve) for model compounds for octahedral and tetrahedral Al^{3+} species, respectively.[28] (b) XANES spectra collected at specific times during heating/cooling. From bottom to top: before starting the heating experiment (parent sample, black curve); at the end of the cooling experiment (blue curve); during the cooling experiment at 488 and 393 K (magenta and dark blue curves, respectively); and at the end of the cooling experiment (violet curve).

agrees with the previous XRPD experiment, where Y zeolite was measured at the beginning and at the end of the heating treatment.[87]

3.2. Aluminum Coordination: Al K-Edge XAS. Figure 3a shows Al K-edge spectra of Na$-$Y and α-Al_2O_3 (corundum), which are typical of tetrahedrally and octahedrally coordinated Al species, respectively.[9,25,27,28,88−92] The absorption edge energy in the spectra of tetrahedrally coordinated Al is about 2 eV lower than that in the spectra of octahedrally coordinated Al. The latter shows a small pre-edge feature and a split white line by about 4 eV. Tetrahedral Al shows a broad feature at about 15$-$20 eV above the edge. On the basis of these features, the evolution of the Al coordination in zeolites as a function of temperature and moisture content was determined.[9,25,27,91,92] Figure 3b shows the Al K-edge XANES recorded at varying temperature in the presence of flowing helium, saturated with water by bubbling through a saturator filled with water of room temperature. The starting sample showed the typical features of tetrahedrally coordinated Al: the white line at 1560 eV and a broad feature 15$-$20 eV above the white line. The features just above the white line are characteristic of tetrahedrally coordinated Al species. The spectrum at high temperature showed only minor changes with respect to that measured at room temperature. The most notable change was the appearance of a pre-edge feature, which has been assigned to undercoordinated Al species, which was probably 3-fold coordinated.[25] Upon cooling, the spectra changed and a loss of intensity of the white line was observed; a small post-edge feature appeared, indicating a change in Al coordination. About 5$-$10% of the tetrahedrally coordinated Al changed to octahedral coordination. A sudden large change in coordination occurred in spectra that were recorded below 393 K in the cooling experiment; there was a dramatic decrease in the tetrahedral white line and a large increase in intensity above the absorption edge, which dominated the spectrum. The broad feature at 15$-$20 eV above the edge also decreased in intensity. This spectrum strongly resembled that of a previously reported USY.[9,92] At this temperature, about 30% of octahedrally coordinated Al had been formed.

3.3. Aluminum Coordination: ^{27}Al MAS NMR. To confirm that structural changes occurred, a fresh batch of $NH_4$$-$Y zeolite was treated under identical conditions and measured with ^{27}Al MAS NMR to determine the Al coordination.[93−97] Figure 4 shows the spectrum of this sample and that of the starting material. The spectra of $NH_4$$-$Y showed two well-defined peaks at around 65 and 0 ppm, corresponding to tetrahedrally and octahedrally coordinated Al, respectively. The starting material contained less than 1% of the octahedrally coordinated Al. After treatment, the peak at around 0 ppm, corresponding to octahedrally coordinated Al, increased in intensity. An additional peak appeared at 33 ppm, typical of distorted tetrahedral species or

(87) Gallezot, P.; Beaumont, R.; Barthomeuf, D. *J. Phys. Chem.* **1974**, *78*, 1550–1553.
(88) Cabaret, D.; Sainctavit, P.; Ildefonse, P.; Calas, G.; Flank, A. M. *Phys. Chem. Miner.* **1996**, *23*, 226–226.
(89) van Bokhoven, J. A.; Koningsberger, D. C.; Ramaker, D. E. *J. Phys.: Condens. Matter* **2001**, *13*, 10383–10398.
(90) van Bokhoven, J. A.; Nabi, T.; Sambe, H.; Ramaker, D. E.; Koningsberger, D. C. *J. Phys.: Condens. Matter* **2001**, *13*, 10247–10260.
(91) van Bokhoven, J. A.; Koningsberger, D. C.; Kunkeler, P.; van Bekkum, H. *J. Catal.* **2002**, *211*, 540–547.
(92) Omegna, A.; Prins, R.; van Bokhoven, J. A. *J. Phys. Chem. B* **2005**, *109*, 9280–9283.
(93) Klinowski, J. *Chem. Rev.* **1991**, *91*, 1459–1479.
(94) Hunger, M. *Catal. Rev.—Sci. Eng.* **1997**, *39*, 345–393.
(95) Fyfe, C. A.; Bretherton, J. L.; Lam, L. Y. *Chem. Commun.* **2000**, 1575–1576.
(96) Fyfe, C. A.; Bretherton, J. L.; Lam, L. Y. *J. Am. Chem. Soc.* **2001**, *123*, 5285–5291.
(97) Jiao, J.; Kanellopoulos, J.; Wang, W.; Ray, S. S.; Foerster, H.; Freude, D.; Hunger, M. *Phys. Chem. Chem. Phys.* **2005**, *7*, 3221–3226.

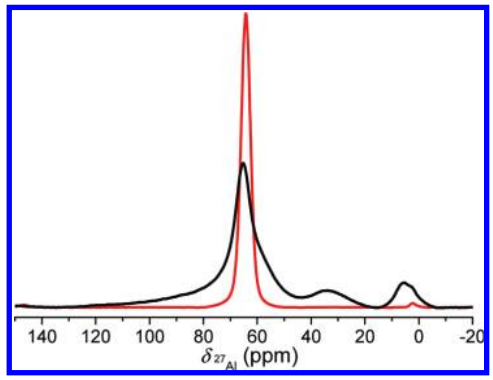

Figure 4. Solid-state ^{27}Al MAS NMR of the zeolite Y measurement at the two extremes: before the heating (red curve) and after the steaming process and successive cooling (black curve).

five-coordinated Al, and the peak at around 65 ppm broadened significantly. The deconvolution of the NMR spectrum of the treated sample showed that 10−15% of the Al atoms are octahedrally coordinated and 10−15% distorted tetrahedrally and five-coordinated.

4. Discussion

The three-dimensional structure of zeolite Y is generated by connecting sodalite units via hexagonal prisms to give a framework characterized by big, empty cavities (supercages) with a diameter of about 13 Å (Figure 1).[32,98−100] Most of the extraframework cations are located at a few well-defined extraframework sites.[101] Site **I** is in the center of the hexagonal prism, closely surrounded by the six oxygens of the two bases of the prism. Site **I′** is located on the external base of the hexagonal prisms, just inside the sodalite cage. These cations are surrounded by three oxygen atoms from the base of the prisms. Sites **II′** and **II** are located in the middle of the six-membered ring forming the boundary between the supercage and the sodalite cage, just inside the sodalite cage and the supercage, respectively.

4.1. Constant Temperature in Situ XRPD Refinements. The Rietveld refinement of the static pattern measured at 873 K (S2 in Scheme 1) was carried out according to standard procedures[32,35] and by optimizing the framework positions first. The Fourier difference maps showed that the refinement was good; there was only a small peak in the electron density of the sodalite cage, just above the hexagonal prism (site **I′** in Figure 1). Because all of the water and ammonia molecules had desorbed from the sample by this stage, the low electron density is attributed to Al^{3+}. A final refinement was made, the results of which are reported in Figure 1b and Table S2. At this stage, 4.3 ± 0.2 of 53.8 Al atoms left the framework. The Al^{3+} occupancy at site **I′** was correlated with that of the Al framework and served to keep the total Al content constant. None of the other cation sites displayed a significant electron density, implying that the remaining cations, needed to balanced the negative charge of the framework, are protons undetectable by XRPD. At this stage, all remaining peaks in the Fourier difference maps were below 0.4 $e^-/Å^3$. The 8% of the extraframework Al species detected by XRPD agrees with the small amounts of undercoordinated Al observed with in situ XAS (Figure 3b).

Table 1. Number of Atoms per Unit Cell in Extraframework Positions (and Corresponding Chemical Assignment) Obtained from the Rietveld Refinement for the Three Static Data Collections Performed with the Whole IP in Isotherm Conditions (Scheme 1)[a]

	number of atoms per unit cell		
extraframework site	S1 (300 K)	S2 (873 K)	S3 (300 K)
Al^{3+}(**I′**)		4.3(2)	18.5(6)
NH_4^+(**I′**)	32(1)		
NH_4^+(**II**)	32(1)		
H_2O(**II**)			25.6(1)
H_2O(**A**)	81(2)		78.7(2)
H_2O(**B**)	92(2)		80.6(2)
H_2O(**C**)	56(1)		40(1)

[a] See Figure 1 for the site nomenclature. The complete sets of optimized parameters and quality factors for the three sets of data are reported in Tables S1−S3 of the Supporting Information.

As expected, the refinement of the pattern of NH_4−Y (S1 in Scheme 1) was inadequate when framework atoms only were included in the model (Figure S2 of the Supporting Information). There are five distinct peaks in the Fourier difference map: **A**, **B**, and **C** are located in the center of the supercage, in positions that are typically occupied by physisorbed water molecules.[34,82] Furthermore, two electron density peaks are near to sites **I′** and **II**, which we attributed to NH_4^+ (Figure 1a and Table S1). Both cationic sites showed full occupancy, resulting in an overall extraframework charge of 64(1) |e| per unit cell as compared to 53.8 as expected from chemical analysis. Thus, a certain fraction of the electron scattering density attributed to NH_4^+ is actually due to water molecules.[102] XRPD revealed a total of 229(3) water molecules per unit cell in the supercage.[94,98,99]

On the basis of our refinements of stages S2 and S1, we performed the refinement of stage S3 (Scheme 1). The Fourier difference map of the refinement of the framework atoms again indicated five extraframework peaks. Sites **A**, **B**, and **C** were once more refined as water molecules, and site **I′** was refined as extraframework Al^{3+}. The cationic site **II** was assigned to water molecules that coordinate a charge-balancing proton, because the dynamic experiment shows that it starts to repopulate at the same time as sites **A**, **B**, and **C** (vide infra, Figure 8). The results of the refinement are reported in Figure 1c and in Table S3. The total amount of readsorbed water was 225(3) per unit cell, in good agreement with the number 229(3) refined for the molecules in the starting material (Table S1).

The Rietveld refinement revealed 18.6(6) Al^{3+} cations per unit cell at site **I′**. This means that approximately 34% of the Al atoms had left the framework during cooling mainly (Table 1). From our in situ XAS measurements, we had assumed that about 30% of the framework Al had been removed. Likewise, ex situ ^{27}Al MAS NMR indicated that about 30% of the distorted or nonframework Al had formed.

4.2. In Situ Time-Resolved XRPD: Standard Refinements. The diffraction patterns collected during heating and cooling (R1 and R2 in Scheme 1) were first refined according to the

(98) Olson, D. H. *J. Phys. Chem.* **1970**, *74*, 2758–2764.
(99) Mortier, W. J. *Compilation of Extraframework Sites in Zeolites*; Butterworth: London, 1982.
(100) Kaduk, J. A. *Cryst. Rev.* **2005**, *11*, 1–19.
(101) Smith, J. V. *Adv. Chem. Ser.* **1971**, *101*, 171–178.

(102) Looking to the evolution of the charge density as a function of temperature in Figure 6, sites **I′** and **II** exhibit two slopes. The first one ends around 400 K, that is, when most of the water molecules leave the framework. It is followed by an almost flat plateau up to 480 K, when the ammonium ions start to decompose. Using the electron density refined in the plateau, a number of 44 NH_4^+ ions per unit cell are refined.

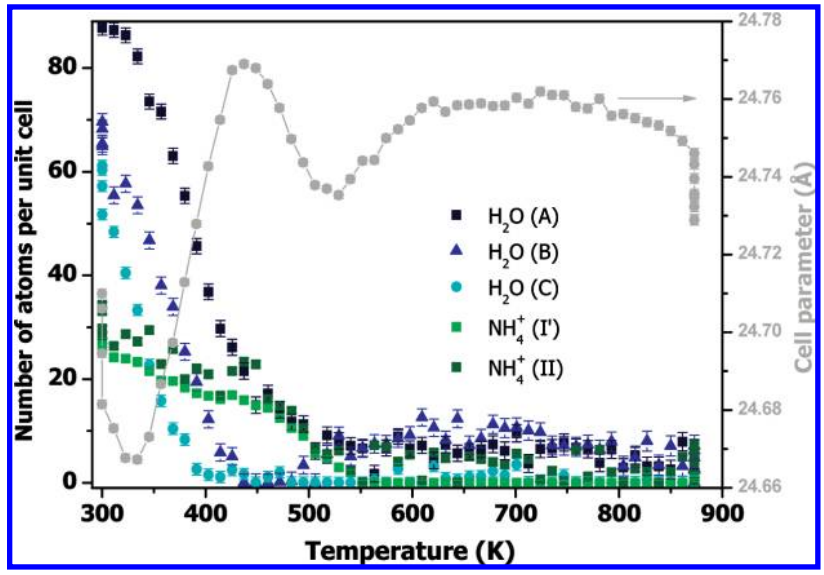

Figure 5. Standard (non parametric) Rietveld refinement. Left ordinate axis: evolution of occupancy factors multiplied by the site symmetry degeneration for the extraframework sites **A**, **B**, and **C** (refined as water molecules) and **I′** and **II** (refined as ammonia cations) versus temperature in the heating experiment (see Figure 1 for location of sites). Right ordinate axis: evolution of the cell parameter. The associated statistical error is always reported. The vertical decrease in the cell parameter at the beginning and end of data collection refer to 4 and 8 points collected in isotherm for 20 and 40 min at 300 and 873 K, respectively (Scheme 1). The same figure reporting the site occupancy factor instead of the number of atoms per unit cell is reported in the Supporting Information (Figure S3).

standard approach,[34,37,55−57,59,62,65−67,103−106] where each diffractogram is considered to be an independent data set. The positions of the extraframework atoms were fixed to the value optimized in the previous analyses: water in sites **A**, **B**, and **C** and NH_4^+ in sites **I′** and **II** (refinement S1, Table S1). For the final refinements, the optimized number of atoms per unit cell of all extraframework sites is reported as a function of temperature, together with the evolution of the cell parameter (Figure 5).

The occupancy factors in Figure 5 allow a description of water release (blue data) and NH_4^+ decomposition with release of NH_3 (green data). These processes take place at 500−550 K. At higher temperature, the single refinements exhibited instabilities, with no meaningful evolution of the occupancy factors. Therefore, we were unable to quantify the remaining extraframework scattering density with the expected extraframework Al^{3+} species. We conclude, therefore, that the standard refinement cannot describe the progressive migration of Al^{3+} species from framework to extraframework positions, which occurred during this steaming experiment. This is due to the correlation among the different optimized parameters, which could not be eliminated because of the overlapping of the peaks typical of powder diffraction and made worse because the data were collected under time-resolved conditions and the fraction of Al^{3+} extraframework species is relatively small.

The behavior of the cell parameters versus temperature (gray curve in Figure 5) is very unusual and is not the consequence of an uncontrolled correlation, as confirmed by its reproduction by means of Le Bail refinement[107] (Figure S6 in the Supporting Information). However, this complex behavior can be interpreted by the parametric Rietveld approach, taking into account the correlation between the different data sets (section 4.3).

4.3. In Situ Time-Resolved XRPD: Parametric Refinements. The standard refinement (R1, Scheme 1) had the following characteristics. The scale factor values plotted against time decreased linearly, correlating to a small part of the exponential curve of the decrease in the current of the synchrotron ring (5 h during the experiment versus current lifetime $\tau = 60$ h). The fractional coordinates x, y, and z of each framework atom (Si/Al, O1, O2, O3, and O4) exhibited a noisy oscillation between the close values obtained in the static S1 and S2 refinements (Tables S1 and S2). Consequently, these 11 parameters were linearly parametrized along the data set. Thus, instead of 682 we refined 22 independent parameters in the 62 patterns. Conversely, the 2θ zero error was refined independently for all 62 patterns to avoid spurious effects on the optimized cell parameter. In all cases, the optimized 2θ zero error was lower than the 10^{-2} absolute zero error, that is, almost zero as compared to the pixel resolution of the IP.

Figure 6 shows the temperature evolution of the unit cell parameter and of the number of atoms per unit cell at all extraframework positions, obtained from parametric refinement[49] during the heating. The parametrized refinement resulted in an impressive improvement in shrinkage of the scattering of the data as compared to the nonparameterized refinement (Figure 5).

Water molecules at site **C** left the framework first, reaching an occupancy of zero at around 410 K. Water molecules at sites **A** and **B** required 450 K to desorb. NH_4^+ cations desorbed from the supercages at 570 K and from the sodalite cages at 670 K. This difference is in agreement with the fact that desorption of NH_3 is hindered by the narrow six-membered windows, through which even H_2 diffuses slowly.[108] At temperatures between 670 and 710 K, the electron density in both the sodalite and the

(103) Martucci, A.; Sacerdoti, M.; Cruciani, G.; Dalconi, C. *Eur. J. Mineral.* **2003**, *15*, 485–493.
(104) Reisner, B. A.; Lee, Y.; Hanson, J. C.; Jones, G. A.; Parise, J. B.; Corbin, D. R.; Toby, B. H.; Freitag, A.; Larese, J. Z.; Kahlenberg, V. *Chem. Commun.* **2000**, 2221–2222.
(105) Sani, A.; Cruciani, G.; Gualtieri, A. F. *Phys. Chem. Miner.* **2002**, *29*, 351–361.
(106) Zanardi, S.; Cruciani, G.; Alberti, A.; Galli, E. *Am. Mineral.* **2004**, *89*, 1033–1042.
(107) Le Bail, A. *Powder Diffr.* **2005**, *20*, 316–326.

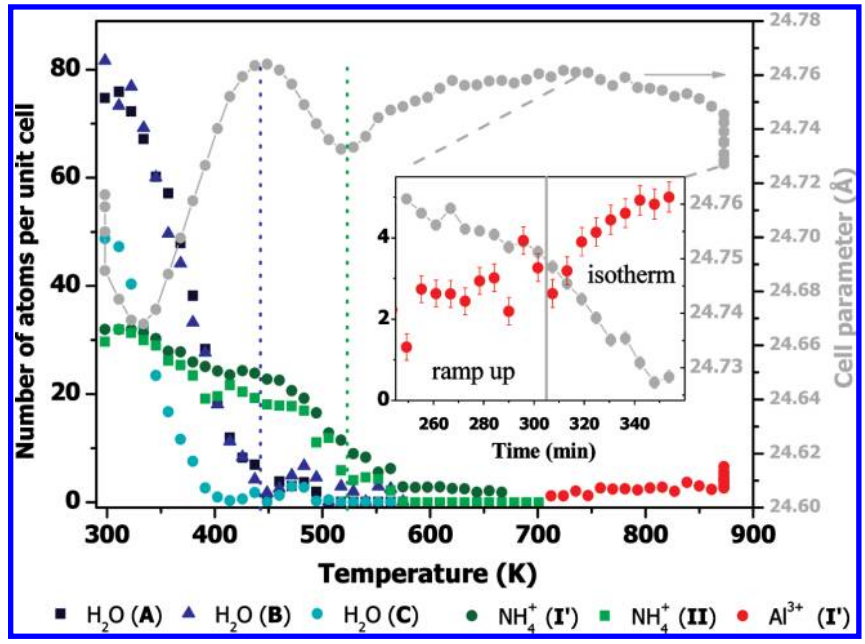

Figure 6. Parametric Rietveld refinement of the heating experiment (R1). Left ordinate axis: evolution of occupancy factors multiplied by site degeneration for the extraframework sites **A**, **B**, and **C** (refined as water molecules) and **I′** and **II** (refined as ammonia cations up to 670 K and as Al^{3+} at higher temperature) versus temperature in the heating experiment (see Figure 1 for location of sites). Right ordinate axis: evolution of the cell parameter. The associated statistical errors (whose values are comparable to or smaller than the size of the symbols) are also reported. Vertical lines represent the correlation of the maximum and minimum evolution with the almost complete evacuation of H_2O and NH_4^+, respectively. The vertical decrease in the cell parameter at the beginning and end of the data collection refers to 4 and 8 points collected for 20′ and 40′ of the isotherm at 300 and 873 K, respectively (Scheme 1). The latter correlates with an increase in the Al^{3+} extraframework occupancy during the high-temperature isotherm. The inset shows the data as a function of time. The same figure reporting the site occupancy factor instead of the number of atoms per unit cell is reported in the Supporting Information (Figure S4).

supercage cavities was close to zero within esd. Above 710 K, limited electron density was found in the sodalite cage. We attributed this density to extraframework Al^{3+}, which started to populate site **I′**. The in situ XAS study (Figure 3b) revealed dislodged aluminum species, which we have now identified as being in the sodalite cage. To quantify these extraframework species from 710 to 873 K, the parametric refinement was modified: instead of the S1 model (Table S1), the S2 (Table S2) model was applied, which has no electron density on sites **A**, **B**, **C**, and **II** but contains Al^{3+} cations at site **I′** at fixed coordinates. This differed slightly (0.24 Å) from those used to refine NH_4^+ at the same site along the 300−710 K data set.

The cell parameter (gray data in Figure 6) shows an alternating decrease and increase. Up to 440 K, the driving force was the framework hydration/dehydration, which caused cell contraction/expansion.[34] During the few minutes at the room temperature isotherm and up to 330 K (Scheme 1), the framework adsorbed additional water molecules due to the higher partial pressure of water under the N_2/H_2O flux. These molecules desorbed from 330 to 440 K, and the unit cell reached a maximum value after all of the water molecules had desorbed (vertical blue line).[34] The successive decrease in *a* was associated with decomposition of NH_4^+, which is equivalent to substitution of a large cation by a small proton. The minimum of *a* at 520 K correlated to the complete depopulation of sites **I′** and **II** (vertical green line). Up to 520 K, thermally induced expansion played a minor role. From 520 to 873 K, all significant transformations have occurred, and *a* showed a typical thermal increase. Finally, during the last few minutes of R1, during which the temperature was constant at 873 K, cell contraction was observed, probably due to the creation of defects, as confirmed by the increase in extraframework Al^{3+} of about 3 to ∼5 atoms/unit cell (inset in Figure 6). Extraframework Al^{3+} reached a maximum of about 6 atoms/unit cell (first point in Figure 8) after 2 h at 873 K (Scheme 1). Thus, prolonged time at high temperature is ineffective at achieving an increase in dealumination.

Figure 7a further confirms the validity of the refinement: the blue line represents the fractional weight loss measured in a TG analysis at the same temperature gradient as compared to the corresponding value extracted from the XRPD parametric refinement (Figure 6). The latter, given in unit atomic mass per unit cell, is obtained from each refined diffractogram by summing the product of the occupancy factor multiplied by the site degeneration and by the corresponding molecular weight over all of the extraframework sites. The scale of the vertical axis for the two measurements was adapted to match the two sets of data, and the abscissa was unchanged. The agreement between the two sets of data is impressive for the whole temperature range; a slight misalignment is observed only at the higher temperatures ($T > 600$ K), where the refinement was done without adding extraframework electron density, while TGA showed a minimal weight loss. A similar trend was found when the template refined fraction was compared to a parallel TG curve in a previous time-dependent synchrotron radiation XRPD study on another zeolitic material.[37] The agreement between the two sets of data is not as good for the cooling experiment because the temperature gradient in the XRPD experiment was not well-defined.

The TGA results show that traces of water are evident in the zeolite channels already at around 500 K, where the sample mass increased by about 3%. This absorption is not revealed by XRPD, for which the measurement of ordered

(108) Scarano, D.; Bordiga, S.; Lamberti, C.; Ricchiardi, G.; Bertarione, S.; Spoto, G. *Appl. Catal., A* **2006**, *307*, 3–12.

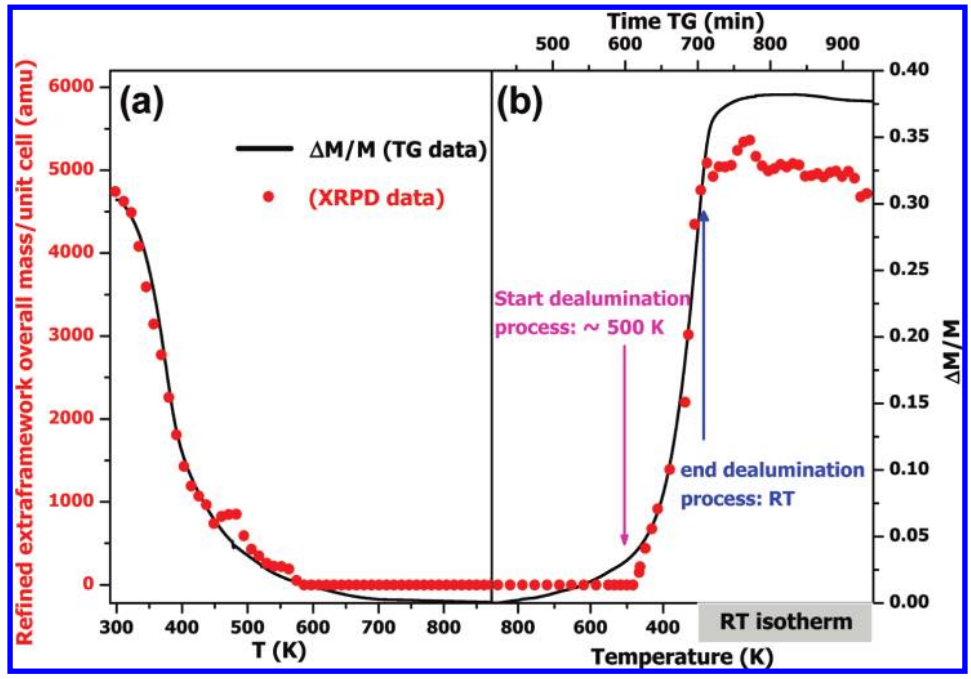

Figure 7. Comparison between the refined overall extraframework mass (scattered red points, left ordinate axis) obtained from XRPD parametric refinement (Figure 6 and Figure 8) and weight loss measured by TGA (solid black line, right ordinate axis): (a) heating; (b) cooling.

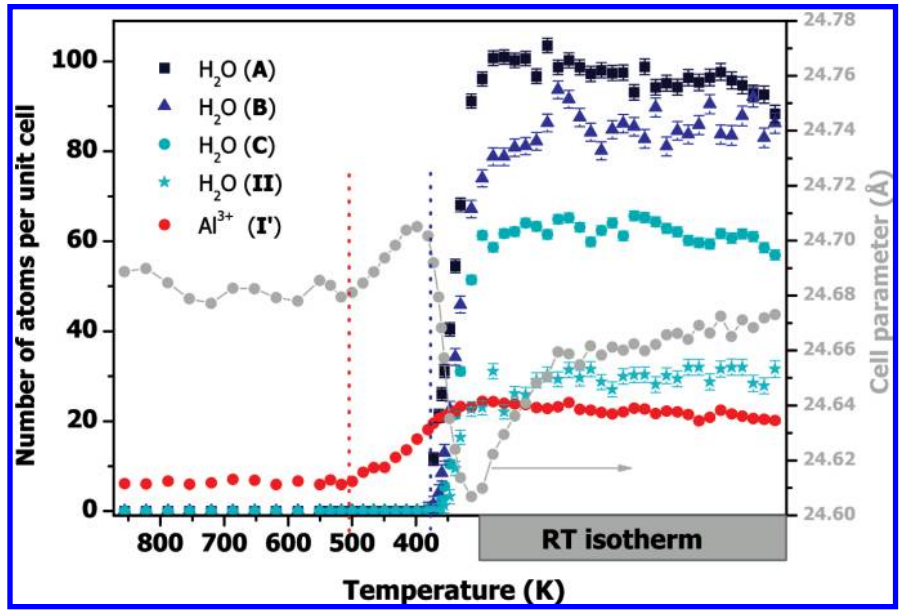

Figure 8. Parametric Rietveld refinement in cooling experiment (R2). Left ordinate axis: evolution of the occupancy factors multiplied by site degeneration at the extraframework sites **A**, **B**, and **C** (refined as water molecules) and **I′** and **II** (refined as Al^{3+} and $H_2O\cdots H^+$ species, respectively) versus temperature in the heating experiment (see Figure 1 for location of sites). Right ordinate axis: evolution of cell parameter *a*. The associated statistical errors are also given. Vertical lines represent the correlations of the start of the increase in *a* with the significant migration of aluminum species into extraframework positions (red curve) and of the successive decrease in *a* with the sudden water uptake by the framework. The same figure showing the site occupancy factor instead of the number of atoms per unit cell is reported in the Supporting Information (Figure S5).

electron scattering density inside the channels begins only at around 450 K.

Figure 8 shows the temperature evolution of the unit cell parameter and of the number of atoms per unit cell at all extraframework positions, obtained from the parametric refinement during cooling. The cell parameter and the Al^{3+} occupancy of site **I′** were constant from 873 to 500 K. Additional electron density was not observed in this temperature range. From 500 to 450 K, there was a concomitant rapid increase in both the lattice parameter and the number of extraframework atoms at site **I′**, from about 6 to about 20 atoms/unit cell. This is compatible with the generation of isolated vacancies, as the volume occupied by 4 OH groups is larger than that occupied by a framework silicon or aluminum atom.[109−111] In this temperature range, a small number of disordered water mol-

(109) Ricchiardi, G.; de Man, A.; Sauer, J. *Phys. Chem. Chem. Phys.* **2000**, *2*, 2195–2204.
(110) Bordiga, S.; Ugliengo, P.; Damin, A.; Lamberti, C.; Spoto, G.; Zecchina, A.; Spanò, G.; Buzzoni, R.; Dalloro, L.; Rivetti, F. *Top. Catal.* **2001**, *15*, 43–52.
(111) Bordiga, S.; Bonino, F.; Damin, A.; Lamberti, C. *Phys. Chem. Chem. Phys.* **2007**, *9*, 4854–4878.

ecules (detected by TGA but not by XRPD, Figure 7b) enters the framework and reacts with Al^{3+} species, causing cleavage of the Si−O−Al bonds and migration to extraframework positions.

From 450 to 300 K, the cell parameter decreased with rehydration of the framework (sites **A**, **B**, **C**, and **II**), in contrast to the increase in this temperature range in the heating experiment (Figure 6). The electron density increased at site **II**, which was populated by NH_4^+ cations in the original material (Table S1) but is now attributed to water molecules coordinated to the Brønsted Si−OH−Al sites hosted at site **II** (Table S3). The centers of mass of two electron densities (NH_4^+ and H_2O) are 0.35 Å apart.

The evolution of the refinement quality parameter R_{wp} during the heating and cooling experiments is reported in Figure S7a and b. In both cases, we observed a small increase/decrease in the quality of the refinement related to water desorption/readsorption; this observation reflects the fact that the dehydrated material is more ordered than the hydrated material. Most importantly, the R_{wp} evolution is continuous, proof that we have correctly followed the structural evolution of the material throughout the process.

4.4. Structural Changes during Heating and Cooling. Our data, showing structural changes, which occur during the heating and cooling of zeolite NH_4−Y under steaming conditions, contradict the generally held view that structural changes occur predominantly at high temperatures. Combining the results of in situ time-resolved TGA with those of XRPD, in situ XAS, and ex situ ^{27}Al MAS NMR, we describe the effect of temperature and water on the framework and extraframework population. During heating NH_4−Y, water and ammonia leave the zeolite, depopulating sites **II**, **A**, **B**, and **C** in the supercages and site **I′** in the sodalite cages. Water molecules at site **C** leave the framework first, reaching zero occupancy at around 410 K. Water molecules at sites **A** and **B** desorb simultaneously at 450 K. NH_4^+ cations in the supercages are depopulated at 570 K and those in the sodalite cages at 670 K. According to TGA and Rietveld refinement, there is a weight loss of about 30% accompanied by minor changes in the aluminum coordination (XAS data). At high temperature, some 3-fold coordinated aluminum probably forms (less than 10%), which populates site **I′**. The main structural changes occur during cooling. XAS shows that down to 393 K about 10% of framework aluminum had changed its coordination and up to 30% during further cooling. According to ^{27}Al MAS NMR, after cooling, 30−35% of aluminum are octahedrally, distorted tetrahedrally, and five-coordinated. These results are in fair agreement with those of Rietveld refinement, which enabled us to locate about 35% of extraframework aluminum after cooling, thus confirming that extraframework aluminum is periodically ordered in the zeolite crystal.

Only minor structural changes occur in the presence of moisture at high temperature; a steady state is reached after 40−50 min at 873 K, and the fraction of extraframework Al^{3+} species increases from about 3 to about 6 atoms/unit cell. These defects are probably the starting points of the large structural changes that occur in the cooling experiment after readsorption of water into the pores, with the fraction of extraframework Al^{3+} species increasing to as much as about 30 atoms/unit cell. In other words, Y zeolite has a partially defective phase; its moisture content is very low at high temperature, and it undergoes further and more important dealumination at lower temperature due to the action of water. Our findings agree with other observations that acidic zeolites are unstable, even at room temperature, when exposed to moisture.[26,27,112]

5. Conclusions

The combination of several techniques (in situ time-resolved XRPD and TG, in situ Al K-edge XAS, and ex situ ^{27}Al MAS NMR) enabled us to determine the atomic scale mechanism of the dealumination of zeolite Y during steaming. These findings represent an important contribution to the understanding of the processes involved in the preparation of ultrastable Y zeolites (USY), the catalyst employed in fluid catalytic cracking (FCC).

Monitoring the dealumination of NH_4−Y zeolite during steaming up to 873 K, we observed that only a small fraction of Al^{3+} species (<10%) left the framework during the heating process to occupy site **I′** inside the sodalite cage. Al K-edge XAS spectra support this finding. The absence of water molecules at high temperature during the heating experiment explains the low efficiency of dealumination at this stage. During cooling, the fraction of extraframework Al increases suddenly, up to about 35% at 500−450 K. TG data show that, in this temperature range, the first water molecules start to repopulate the framework. Such molecules are the driving force of the dislodgment of most of the Al from the zeolitic framework. The convergence of all three employed techniques (the structural ones working at different length scales) assures that the obtained picture of the dealumination reaction is correct, even if some technique was sometime pushed close to its limits, that is, XRPD measuring the occupancy of low populated Al extraframework sites and XANES working under in situ conditions at so low photon energy (Al K-edge).

The standard Rietveld refinement (Figure 5), which includes all XRPD patterns collected during heating and cooling as independent data sets, monitored the considerable electron density depopulation/population processes such as water desorption/adsorption and NH_4^+ decomposition but revealed nothing about the weak aluminum dislodgment in the extraframework position. This dislodgment could be understood by analyzing the XRPD data by means of the innovative parametric refinement,[49] which includes all of the XRPD patterns collected in time-resolved experiments as an unique data set. This methodology significantly increases the statistics, reduces the overall number of optimized variables and, thus, their relative correlation, and finally results in a more reliable estimate of the optimized parameters. This approach located the extraframework Al species, whereas the standard procedure failed.

Through the use of sophisticated synchrotron radiation techniques, it has recently been shown that it is possible to discriminate between Si and Al occupancies in crystallographically independent framework T sites (i.e., the catalytic Brønsted sites have been located in the unit cell).[113] In the present work, we have shown that it is also possible to follow the framework Al depopulation and the increase of extraframework Al^{3+} Lewis sites.

Acknowledgment. We are indebted to the staff of GILDA BM8 at the ESRF (in particular to M. Merlini, C. Meneghini, and F. D'Acapito) and of LUCIA at the SLS (in particular to R. Wetter) beamlines for their competent support during the XRPD and XAFS

(112) Omegna, A.; van Bokhoven, J. A.; Prins, R. *J. Phys. Chem. B* **2003**, *107*, 8854–8860.
(113) van Bokhoven, J. A.; Lee, T.-L.; Drakopoulos, M.; Lamberti, C.; Thiess, S.; Zegenhagen, J. *Nat. Mater.* **2008**, *7*, 551–555.

measurements, respectively. C. Prestipino is acknowledged for his assistance during the XRPD data collection and G. J. Vitillo for her assistance in the preparation of the model of zeolite Y (Figure 1). J.A.v.B. and N.D. thank the Swiss National Science Foundation for financial support. C.L. is thankful for support from the MaMaSELF consortium (http://etudes.univ-rennes1.fr/mamaself).

Supporting Information Available: Schemes and photos of the in situ, time-resolved XRPD experimental setup used at the GILDA BM8 beamline of the ESRF; calculated and residual XRPD patterns simulating the S1 static pattern (Scheme 1) with only framework atoms; complete sets of optimized parameters and quality factors obtained in the Rietveld refinement of the static patterns S1, S2, and S3 in Scheme 1; the results given in Figures 5, 6, and 8 of the main text, where the number of atoms per unit cell is reported instead of the site occupancy factor; comparison of the evolution of the cell parameter throughout the heating and cooling experiments obtained by Le Bail and Rietveld refinements; and evolution of the R_{wp} parameter during heating and cooling. This material is available free of charge via the Internet at http://pubs.acs.org.

JA907696H